HIGH ORDER CFD-SIMULATION OF THE ROTOR-FUSELAGE INTERACTION

Ulrich Kowarsch, Manuel Keßler and Ewald Krämer
kowarsch@iag.uni-stuttgart.de, University of Stuttgart, IAG, Pfaffenwaldring 21, Stuttgart, 70569, Germany

Abstract

The presented paper investigates a fluid-structure interaction phenomenon of a helicopter in fast forward flight, called tail shake phenomenon. Due to the interaction of the rotor wake with the tail boom, a high vibration level is introduced under unfavorable conditions. The current problem to simulate this phenomenon using a Computational Fluid Dynamics (CFD) code is the too low preservation of the rotor wake to resolve the interaction with the structure. In order to resolve this drawback, the CFD Code FLOWer was extended with a fifth order Weighted Essentially Non-Oscillatory (WENO) state reconstruction scheme for an improved rotor wake conservation. In addition, the flux reconstruction is solved using a Lax-Friedrich or a HLLC Riemann solver. The tail shake phenomenon is simulated on the basis of the European joint wind tunnel measurement campaign GoAHEAD. The variety of provided experimental data allows a detailed comparison with the CFD simulation and an evaluation of the CFD methods. The simulation is performed under the usage of the FLOWer standard scheme and newly implemented high order scheme with the two Riemann solvers to show their benefits in comparison to the experimental data. It is shown, that the higher order scheme gives a significant improvement in conserving the rotor wake, especially with the usage of the HLLC Riemann solver. The structure of the flow field shows accordance in several flow characteristics like pressure, vortex positions and integral forces. In addition, it is shown that the influence of the rotor hub wake to the structural forces and moments is significant.

NOMENCLATURE

CFD	Computational Fluid Dynamics
DLR	Deutsches Zentrum für Luft- und Raumfahrt e.V.
IAG	Institute of Aerodynamics and Gas Dynamics
JST	Jameson Schmidt Turkel
RANS	Reynolds averaged Navier Stokes
WENO	Weighted Essentially Non-Oscillatory

1 INTRODUCTION

The numerical investigation of interaction phenomenon problems is still one of the to date unsolved issues in helicopter aerodynamics. An example for that is the rotor-fuselage interaction, which is also called the tail shake phenomenon[1]. This interaction can occur in fast forward flight, where the main rotor wake interaction with the tail boom and the fin of the fuselage causes a fluctuation of the lateral moment. If this excitation is close to a lateral elastic mode of the fuselage structure, a high vibration level is caused with undesirable random character, which is felt by the flight crew as lateral "kicks"[1]. Up to now, CFD methods are not capable of predicting the occurrence of this phenomenon and the characteristics of the interaction. Therefore even well known helicopter types as the Boeing AH-64D Longbow Apache[2] and the Eurocopter EC135[3] showed this phenomenon during the early flight test phase with corresponding mitigation efforts and cost.

In order to overcome this drawback, the capability of the structured CFD solver FLOWer from DLR[4], which is extensively used at the Institute of Aerodynamics and Gasdynamics (IAG) of the University of Stuttgart, is investigated to simulate the tail shake phenomenon. To improve the solver for this task, the CFD code was advanced with a spatial higher order WENO scheme in combination with different Riemann solvers for a better vortex preservation, which is essential for a rotor-structure interaction.

The validation of the CFD simulation is done with a comparison to the GoAHEAD wind tunnel experiment[5], which provides extensive flow data of a helicopter model in tail shake condition.

To quantify the benefit of the higher order scheme compared to the common second order scheme, the simulation is performed with both schemes and compared. In contrast to previous helicopter simulations, a modeling of the rotor blade connections is done to resolve the rotor hub wake as detailed as possible, which has significant impact on the tail shake phenomenon as described in[1].

2 NUMERICAL METHODS

2.1 CFD method

The aerodynamic solution is computed with the CFD code FLOWer[4], which was developed by the German Aerospace Center (DLR). The code discretizes the unsteady Reynolds-averaged Navier Stokes equations with a spatial second order central difference scheme for flux computation according to Jameson, Schmidt, and Turkel (JST)[6]. This flux computation was extended by the Institute of Aerodynamics and Gas Dynamics to a fifth-order WENO flow state reconstruction scheme according to[7] in combination with a Riemann solver. Two Riemann solvers were implemented, the one-wave model Lax-Friedrich (denoted as WENO-LF) and the upwind HLLC flux scheme (denoted as WENO-HLLC) according to[8]. A detailed review of the implementation and validation can be found in[9] and[10]. The consideration of relative grid movements using an Arbitrary Lagrangian Eulerian (ALE) approach enables the code for helicopter flow simulation. In addition, the Chimera technique for overset grids enables the meshing of complex helicopter geometries like rotor-fuselage configurations and the relative grid movement. To consider the effects of fluid-structure interaction to the rotor blade, the mesh is deformed to a given structural deformation of the blade for each time step. The efficiency of the computation is achieved by a multi-block structure of the grid to enable parallel computing. The RANS equations are closed by the use of the Wilcox k-ω turbulence model according to[11].

2.2 CFD-CSD coupling

The computation of the structural response of the main rotor blades is performed with the Eurocopter inhouse code HOST[12] and weakly coupled to FLOWer. HOST models the rotor blade as an Euler-Bernoulli beam with rigid elements, which are connected by virtual joints to compute the structural response to the aerodynamic forces. The rotor aerodynamics in the HOST code is approximated with a two dimensional Blade Element Theory (BET). The coupling is conducted by providing the aerodynamic forces F_{CFD} of the CFD calculation to the CSD code to compute the structural response. Additionally, HOST ensures that specified rotor forces and moments, the so called trim objectives, are met by adjusting the helicopter control inputs collective, lateral and longitudinal cyclic pitch. The trim process underlies the approach

$$F_{HOST}^{n+1} = F_{2D}^{n+1} - (F_{CFD}^{n} - F_{2D}^{n}) \quad (1)$$

with F_{2D} being the HOST internal forces computed on the basis of the two dimensional BET and F_{HOST}^{n+1} the forces used to determine the trim objectives for the new iteration step $n+1$. A converged state is reached if F_{2D}^{n} equals F_{2D}^{n+1} and thus the force F_{HOST}^{n+1} depends then only on the CFD computed forces F_{CFD}^{n}.

3 GOAHEAD PROJECT

With the aim to provide a helicopter database for CFD code validation the GoAHEAD project[5] was formed to evaluate the physical quality of a CFD simulation. The model configuration equals a modern transport helicopter (cf. figure 1), including a full controllable main rotor, fuselage and a tail rotor. The configuration had a length of $4.15\,\mathrm{m}$ and a clockwise rotating main rotor with a diameter of $4.20\,\mathrm{m}$ and four rotor blades. The rotation frequency of the main rotor was set to $15.95\,\mathrm{Hz}$ leading to a blade tip mach speed of 0.617. The two bladed tail rotor with a diameter of $0.383\,\mathrm{m}$ was operated with a rotation frequency of $79.77\,\mathrm{Hz}$, leading to a 5 times higher rotation frequency as the main rotor. A large wind tunnel campaign was

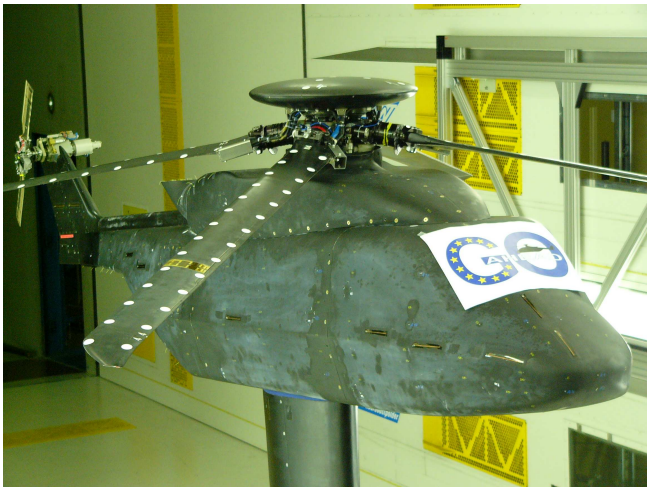

Fig. 1. GoAHEAD helicopter model in the DNW wind tunnel

conducted for different flight states with focus on distinctive helicopter phenomena in the DNW LLF wind tunnel in Marknesse, Netherlands. One flight state was inter alia the fast forward flight under tail shake condition. An overview of the flow states of the tail shake flight condition is listed in table 1.

The provided experimental data cover global forces, steady and unsteady pressures, transition positions, stream lines, position of flow separation, velocity fields in the wake, vortex trajectories and elastic deformations of the main rotor blades. Investigating the tail shake phenomenon, the unsteady pressure measurements and PIV recordings of areas around the tail boom are focused.

Test case	TC4 tail-shake
Database record no.	396
Wind tunnel mach number [-]	0.204
Fuselage pitch [°]	2.5
Main rotor shaft inclination [°]	7.5
Main rotor thrust coefficient C_T/σ_{MR} [-]	0.071
Tail rotor thrust coefficient C_T/σ_{TR} [-]	0.081

Table 1. GoAHEAD experimental data references and wind tunnel/ model conditions.

4 SETUP AND SIMULATION

The simulation of the tail shake phenomenon requires a highly detailed resolution of the flow topology and therefore a detailed modeling of the helicopter's geometry. In contrast to most of the past helicopter simulations, the rotor hub and the blade connections are taken into account in this research to consider their effects on the rotor wake and further on the fuselage. To enable the structured meshing of the rotor hub, the overset grid method is used and the geometry is divided into several sections to allow a reasonable grid quality. Figure 2 shows the complete helicopter geometry with the colored grid components which are separately meshed. The cylindrical approximation of the rotor hub core is justified with the high amount of measure instruments mounted around the rotor mast (cf. figure 1). The gapless transition between rotor hub and rotor blade is realized with a blade root mesh which performs a grinding pitching movement on the shared surface between rotor hub and blade. The blade deformation is applied after the connection between hub and blade in the blade root mesh. A minor error is introduced with the appliance of the blade deformation first in the blade root grid since lag hinge and flap bearing are more inboard. This leads to a point of inflection when adapting the deformation initially at the blade root grid.

The meshes of the helicopter model are embedded

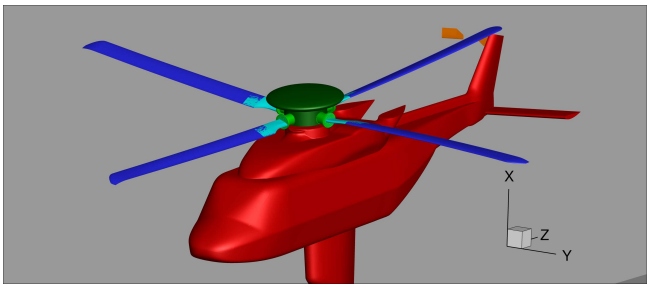

Fig. 2. Separately meshed geometrical components of the GoAHEAD helicopter model

Component	No. of blocks	No. of cells
Fuselage	359	18,443,136
Rotorhub	405	13,377,536
Rotorhub arm	4× 38	4× 1,220,608
Background	450	20,123,648
Main rotor blade	4× 45	4× 1,330,624
Main rotor blade root	4× 12	4× 817,152
Tail rotor blade	2× 30	2× 648,192
Total	**1654**	**66,714,240**

Table 2. Grid system of the CFD setup.

in a Cartesian background mesh, which is bounded by the wind tunnel walls in x- and y-direction. The expansion of the background mesh in front and behind the model is chosen 2.5 rotor diameters to avoid flow interactions with the boundary condition. In case of a computation using WENO, the scheme is only applied for the Cartesian background mesh to achieve an improved rotor wake conservation. A higher order computation in the structural grids is put aside due to the higher computational effort with marginal accuracy improvement in the highly resolved structure grid. Table 2 lists the grid system used in this setup.

4.1 Trim convergence

In order to achieve a fast converged solution with faded start-up effects, the simulation was started with the computationally less expensive second order JST scheme for the complete mesh. The first trim iteration was started after 4 complete rotor revolutions were computed, to ensure a flow field without start up effects. In order to investigate the influence of the different flux computation schemes, the trim process was performed until a converged state was achieved using the JST scheme. The convergence lasts for 11 trim iterations, with 0.75 rotor revolution between each trim leading to a summed computation of 12 rotor revolutions (cf. figure 3). Contrary to isolated rotor computations (cf. [13]) the trim process lasts double times to reach a converged state which is justified with the more complex flow field. Afterwards the computation was continued using the WENO-LF and WENO-HLLC scheme for 2 rotor revolutions. According to the inflow velocity the rotor wake passes the fuselage within this time, so that a complete WENO computed rotor wake in the area of concern is present. A further trim iteration was performed in order to investigate the influence of the higher order scheme. Figure 3 shows the 12th trim iteration as the WENO trim which shows no change in the trim objectives of relevance. The WENO-HLLC and WENO-LF trim show the same control angles with deviations less than $0.0025°$ and are therefore shown in one common WENO trim. The results show satisfying accordance to the experimental control angels. In case of the collective pitch angle a deviation of $0.85°$ is present. Other investigations

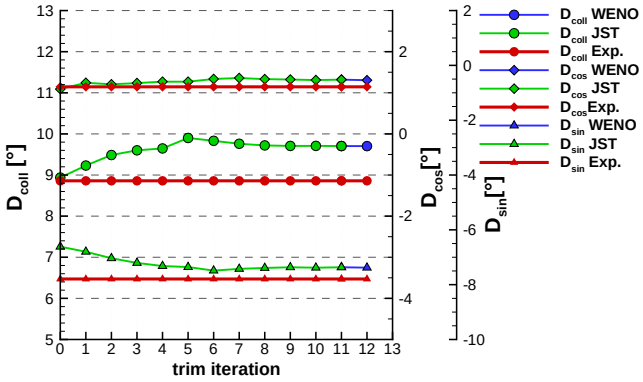

Fig. 3. Progression of the rotor control angles during the trim process

using the structure dynamic code HOST showed the same behavior[13] with deviations in the collective of about 1°. The tail rotor thrust was adjusted manually by modifying the tail rotor blades collective angle until an equal rotor thrust between experiment and CFD computation is achieved in the mean thrust value.

4.2 Simulation and evaluation window

After the trim was performed for each case, the simulation was continued for 3 more rotor revolutions, which are used for the investigation of the flow field and comparison to the experimental data. Especially with focus on the unsteady pressure sensors, surface pressure values were written out each time step (1°), which gives the capability to resolve frequencies reliable up to 180/rev according to the Nyquist criterion. The simulation was performed on the CRAY XE6 HERMIT cluster at the High Performance Computing Center (HLRS) in Stuttgart using 1024 cores. The time step was set to 1° of the main rotor revolution for the computation with up to 70 iterations per time step depending on the minimal required pressure residual set to $1 \cdot 10^{-4}$. With the computation of 12 trimmed JST revolutions, 2 convective revolutions for the WENO schemes, and 3 further for each method a summary of 25 rotor revolutions had to be computed. The computational cost was 12% higher using the WENO-LF scheme and 16% higher using the WENO-HLLC scheme compared to the second order JST scheme. One rotor revolution using the JST scheme required 51438 CPU hours giving a summary of approximately 1.4 million CPU hours for the total simulation campaign.

5 NUMERICAL RESULTS

Figure 4 shows the in plane voriticity of a instantaneous slice through the y symmetry plane of the helicopter with stream traces. The topology shows accordance with the typical characteristic after[1], where the rotor hub wake propagates in a flat angle to the fuselage and hits the tail boom and tail fin. In addition, the figure shows the structure of the wake which is characterized by small scale vortices arising at the rotor hub and the blade connections. This reveals the need of the detailed rotor hub modeling to resolve these small scaled vortex topology influencing the wake propagating to the tail boom.

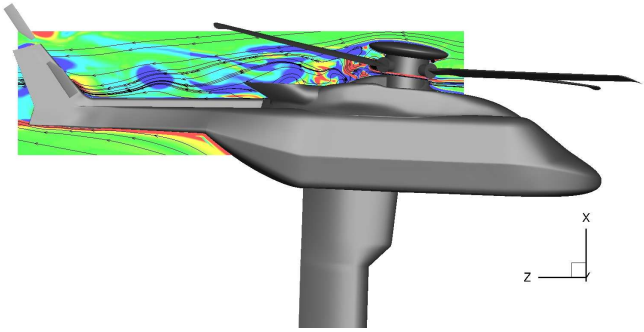

Fig. 4. Instantaneous in plane vorticity topology in the y symmetry plane area around the rotor hub and tail boom (16^{th} rotor revolution at $\Psi = 45^\circ$, WENO-HLLC computation)

For a comparison of the different numerical schemes, the iso-surface of the λ_2-criterion is analyzed, to get an overview of the improvement of vortex preservation. Therefore an instantaneous λ_2 iso-surface after 16 rotor revolutions is sown in figure 5 for the same value of λ_2 for all three different schemes. The surface is colored with the location of the vortex in x direction, the origin being placed in the undeformed rotor disk plane. The topology of the flow is characterized by the rotor tip vortices, but in the tail boom area the rotor hub wake, which shows a highly swirled flow field, is dominant. The significant loss of vortex preservation in the area behind the helicopter is caused by a substantial grid coarsening, making use of hanging grid nodes. In addition, in this area of no concern the flux computation scheme is switched to JST for all cases. The comparison is shown to assess the advantage of a high order flux reconstruction. In several areas the better vortex conservation is apparent using the higher order schemes. Compared to the second order JST schemes, the WENO computations shows significantly lower numerical dissipation,observable by a more discrete conservation of the vortex in the region of the blade tip vortices and rotor hub wake. Especially with the time propagation of the blade tip vortices, the significant improvement is visible where in case of the WENO-HLLC computation a well defined vortex core is preserved. In addition, the lower numerical diffusion is made clear at the path of the rotor tip vortex in front of the helicopter, where in case of the JST scheme several out of vortex fragments can be

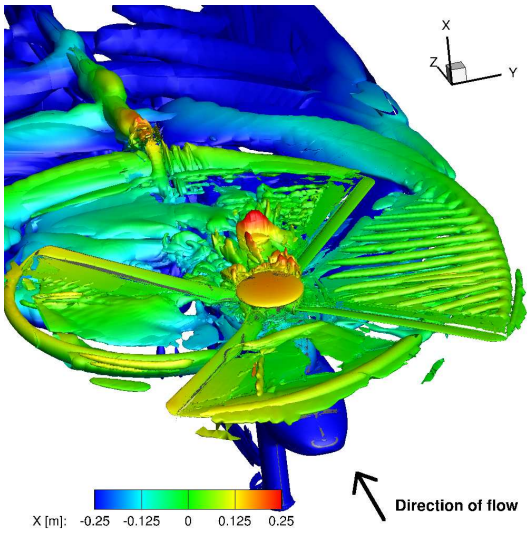

(a) 2^{nd} order JST

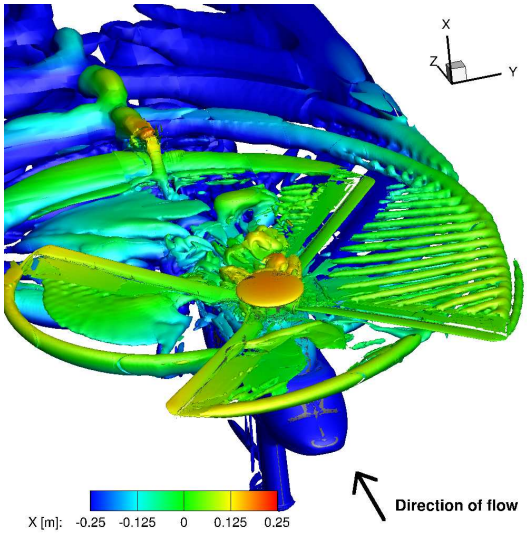

(b) 5^{th} order WENO-LF

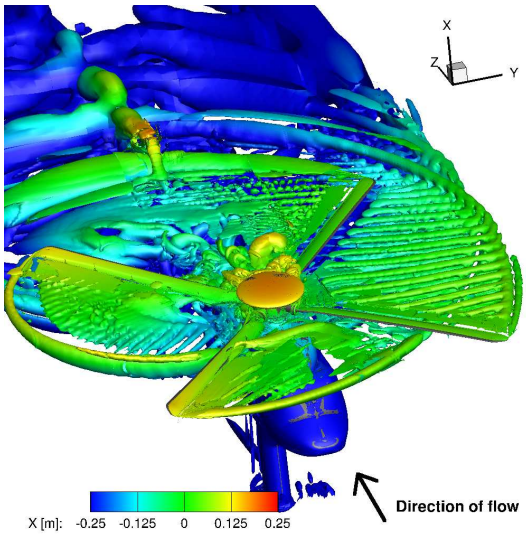

(c) 5^{th} order WENO-HLLC

Fig. 5. Instantaneous λ_2-visualization of the vortex topology (16^{th} rotor revolution at $\Psi = 45°$)

found despite the same λ_2 visualization settings. The three λ_2 iso-surfaces cover the recognition of former FLOWer WENO investigations (cf.[10]), where wake conservation is more significantly improved between WENO-LF and WENO-HLLC than between JST and WENO-LF.
Remarkable in all cases are vortexes rolling up in the shear layer of the rotor blade, especially in case of the advancing blade (note the clockwise sense of rotation). Investigations revealed that this is a fragment of the second order chimera interpolation, which leads to an unbalance of the shear layer strength having this periodic roll up effect as a consequence. Since the error occurs in all three cases, this effect is separated from the usage of the flux computation order. Anyway, investigations have been launched in order to get rid of this numerical error, which already show that this is a problem only during fast forward flight. The influence of this error to the tail shake investigation is expected to be minor, since the strength of this disturbances are small compared to other vortices. Hence it is to be denoted, that the higher vortex preservation also transports the disturbances longer.

5.1 Comparison with the experimental data

The data set of the GOAHEAD experiment covers integral fuselage forces, unsteady pressure measurements and PIV records in the tail boom region. In this chapter these data sets are compared with the CFD data to investigate the reproduction quality of the flow field phenomena.

5.1.1 Integral fuselage forces

Initially, the integral forces on the fuselage of the CFD simulations are compared to the experimental data. Therefore, the x-,y-, and z-oriented forces in the fuselage coordinates (inclination of $2.5°$ around Y-axis) are shown in figure 6. The forces are phase averaged to a full rotor revolution in order to resolve rotor harmonics beside multiples of the blade passing frequency. The force developments of the CFD computation uses the 3 evaluation revolutions, whereas the experimental progression is computed out of 32 recorded revolutions. The forces include the tail rotor thrust, as the tail rotor was mounted on the fuselage in the experiment in contrast to the main rotor.
In case of the force component in x-direction (F_x) an offset of the mean force of around $125\,\mathrm{N}$ is found. In addition, an azimuthal phase lagging of around $20°$ behind the experimental data is found. Hence the unsteady behavior of the progression shows a reasonable accordance in the 4/rev as well as higher harmonic fluctuations of the force. This is notable at $\psi = 120°$ where a higher harmonic fluctuation appears at the peak of the 4/rev oscillation. Between

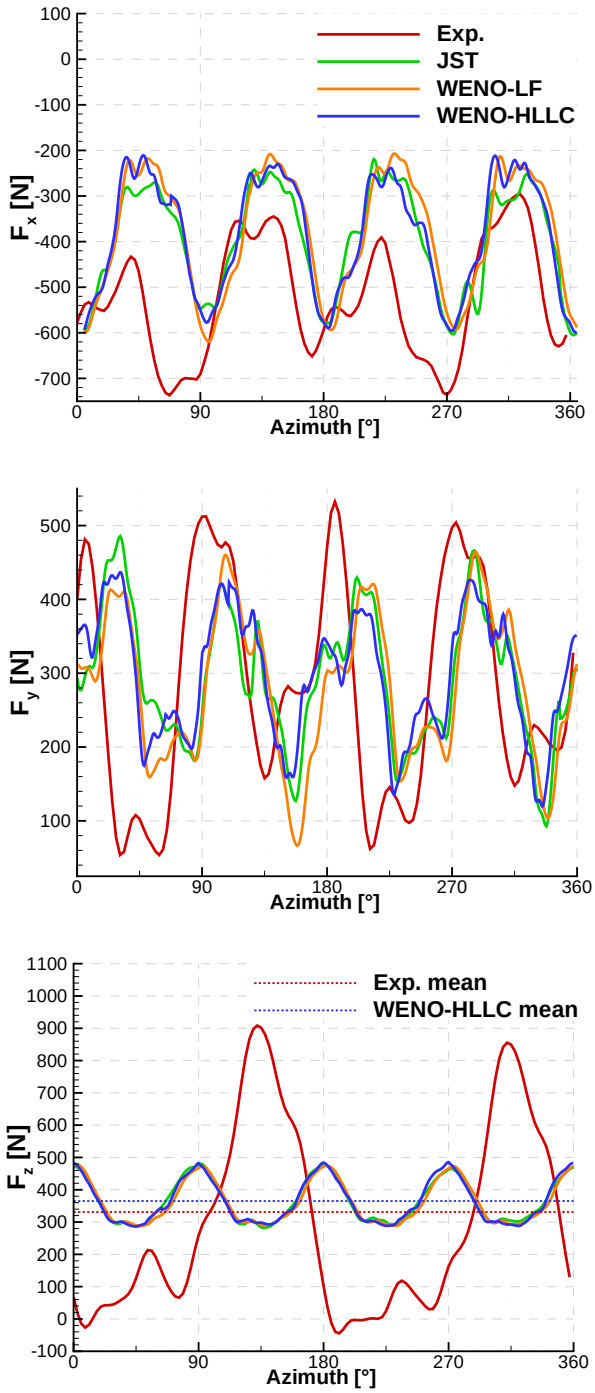

Fig. 6. Phase averaged integral forces on the fuselage.

$\psi = 180^\circ$ and $\psi = 225^\circ$ during the high 4/rev gradient a higher harmonic fluctuation is found to be influencing the force the same way in the CFD as well as in the experimental data. With focus on the tail shake phenomenon, the lateral force component F_y is of higher relevance. The comparison shows more parts of higher harmonic oscillations founded inter alia in the addition of the tail rotor thrust. In this case the mean force value is met, but with a lower amplitude. As found in the F_x force component, an azimuthal phase lag of about 20° is present. The force component F_z displays contrary to the x- and y-directed forces significant deviations. The experimental data shows a distinctive 2/rev oscillation which is unexpected for this kind of helicopter configuration in the longitudinal direction. The GoAHEAD deliverable describes the cause of this oscillation as the consequence of probably tip path plane splitting, which causes this 2/rev fluctuation in the force which is measured by strain gauges. Apart from the 2/rev oscillation, the mean values (drawn as dotted lines in the figure) of the data shows high accordance with a deviation of $30\,\mathrm{N}$. Hence, due to the possibility of significant errors in the F_z experimental measurement a further evaluation of the F_z force component is foreseen.

For a comparison of the higher harmonic fluctuation the signal is displaced with $\delta\psi = 20^\circ$ and shown in figure 7. The higher harmonic oscillations are found to have the same characteristics as the experimental data without any further errors in the phase angle.

For a more detailed comparison of the frequency

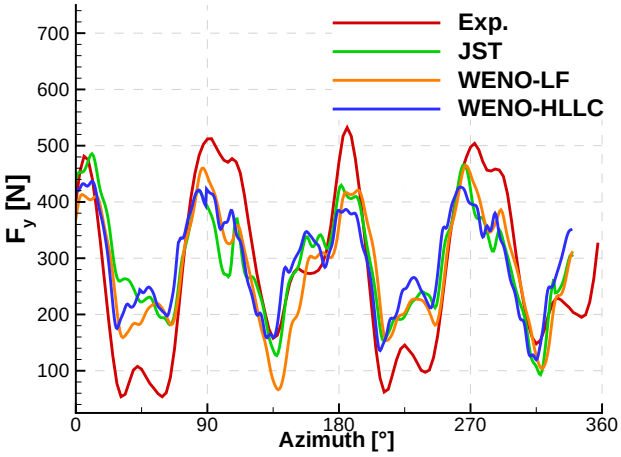

Fig. 7. Integral fuselage force in y-direction with a phase sweep of $\delta\psi = -20^\circ$ in the CFD signal

components the Fast Fourier Transformation (FFT) of the phase averaged signals are shown in figure 8. The FFT reveals for the force component F_x a significant 2/rev amplitude in the experimental data. Even if the overlay of the 4/rev main rotor oscillation and the 10/rev tail rotor oscillation can give a 2/rev periodic fluctuation, this significant amplitude is suspected to root at the same cause as for the oscillation in F_z. The amplitudes of the 4/rev frequencies are in the same scale with variations of around 20%. For higher frequencies, the CFD data differs clearly in the 10/rev frequency, where in the opposite to the experimental data, no excitation is found. The occurrence of the 10/rev frequency, mainly excited by the tail rotor, is unexpected to have this high influence to the vertical force F_x. For the 8/rev frequency, the frequency spec-

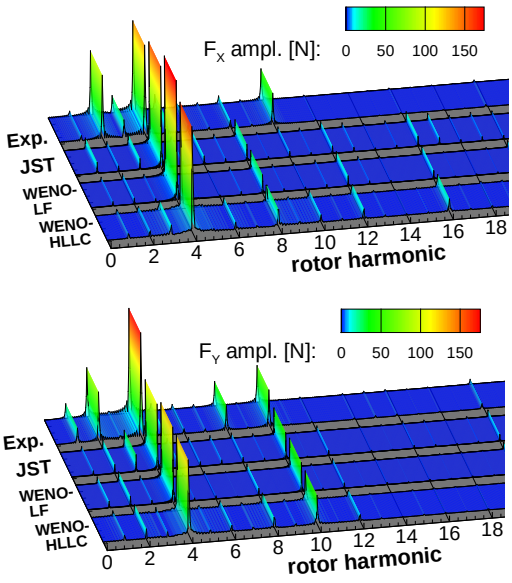

Fig. 8. Fast Fourier Transformation of the fuselage force signals

trum between CFD and experiment is vice versa with a higher frequency amplitude of the CFD data.
The force component F_y shows similar characteristics, with a notable 2/rev frequency in the experiment. The 4/rev amplitude is under estimated by the CFD computation as already seen in the time developments. The amplitude of the 10/rev oscillation in contrast is remarkable precisely met.
In the appendix, figure 22 shows the standard deviation of the forces for the experiment marked as dotted lines. Representative for the CFD computation, the standard deviation for the JST computation is shown as well. The small deviations confirm the assumption to investigate the phase averaged development for the frequency analysis. The highest deviation is found in the F_y force component for the CFD computation influenced by higher harmonic oscillations. Further, the undesired 2/rev signal in the F_z force component in the experiment remains stable over the complete measurement window.

5.1.2 PIV planes

Exemplary for the PIV measurement data of the experiment, figure 10 shows a comparison of the JST, WENO-LF, WENO-HLLC, and experimental data for a PIV-slice in the region of the tail boom (cf. figure 9). The contour shows the absolute velocity magnitude with in-plane velocity stream traces. The CFD data are phase averaged for the 22.5° azimuth position over the 3 evaluation rotations. The experimental data is averaged over 47 rotor revolutions for the same azimuth angle.
The CFD methods show the same characteristics of the flow topology with the same behavior as in case of the λ_2 plot. The superiority of the WENO methods in preserving vortices and causing lower dissipation in comparison to the JST method is obvious, which leads to stronger preserved vortices. This is especially made clear in the region of negative y-direction where between the CFD methods a significant improvement of the preservation of a prominent vortex is found. The experimental data shows a wake which

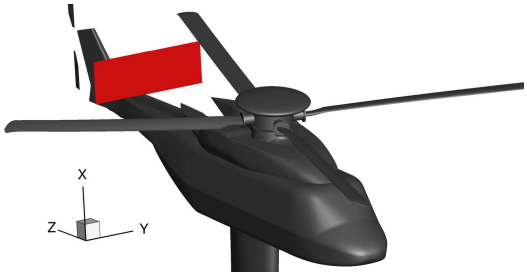

Fig. 9. Location of PIV-plane (GoAHEAD experimental notation: PIV01SP05R01-02)

seems primarily be formed by the striking turbine outlets. Two vortices on both sides are present, formed by the wing tip shaped turbine outlets superimposed with the downwash by the rotor according to the rotors direction of rotation from right above to lower left. In addition, an asymmetry for the y-axis is clearly found with a stronger vortex starboard sided.
Comparing the flow structure with the experimental data, the topology shows accordance in the border of the wake, which shows improvements using the WENO-HLLC method. The starboard sided vortex appearing in the experimental data is reproduced in case of the WENO-LF and more discrete using the WENO-HLLC scheme. The JST schemes lacks the reproduction of the negative y-directed section. The outer boundary of the wake structured is approximated, hence not reproduced sufficient to find the same characteristics. In case of the backboard located vortex no CFD computation shows accordance with the experiment. Even if a vortex is present and in its strength preserved with the WENO-HLLC method, the sense of rotation is contrary the vortex in the experiment. The location in the CFD at $Y = 0.2\,\mathrm{m}$ differs also from the experimental data at $Y = 0.35\,\mathrm{m}$.

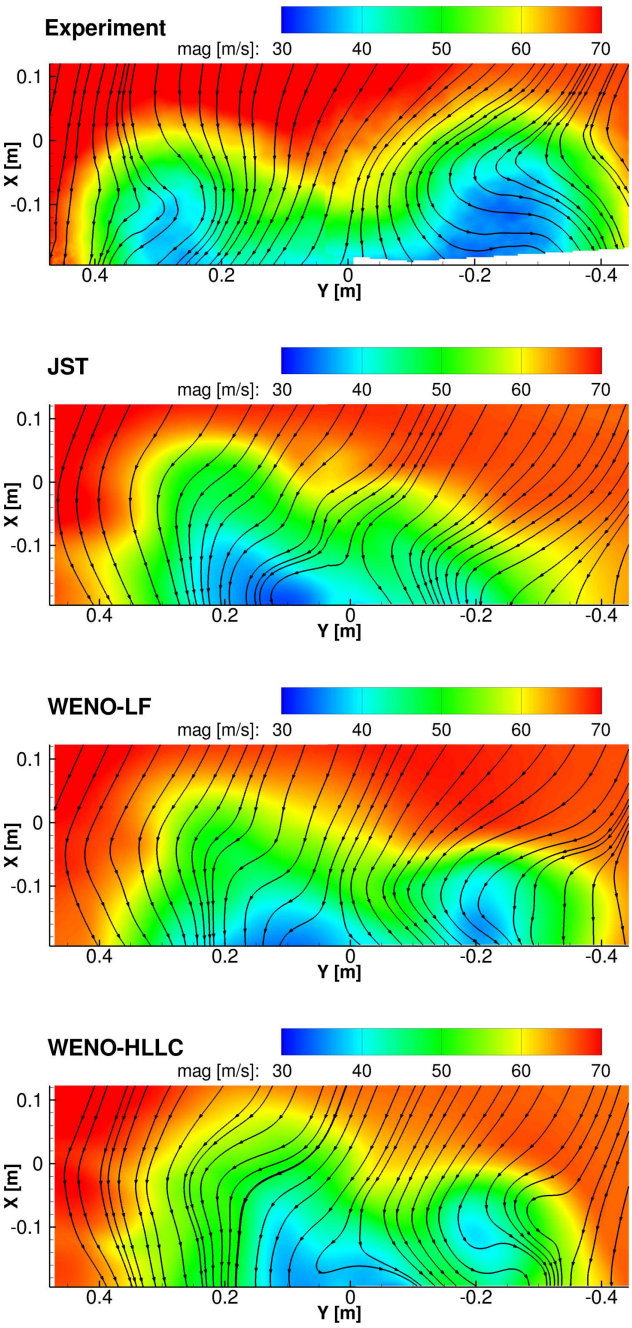

Fig. 10. Comparison of azimuthal averaged velocity fields at $\Psi = 22.5°$ over 3 revolutions in case of CFD and 47 revolutions in case of experimental data. (view from behind)

5.1.3 Unsteady pressure sensors on the fuselage

The experimental data provides measurement data of 131 unsteady pressure sensors distributed over the fuselage shown in figure 11. In case of the CFD computation the sensor data was recorded for each $1°$ azimuthal time step, leading to a sampling frequency of $5752.2\,\mathrm{Hz}$. The discrete data at the

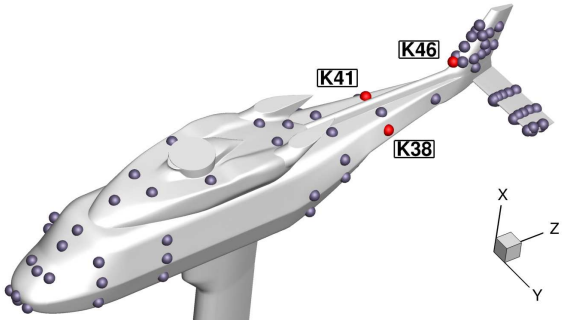

Fig. 11. Locations of unsteady pressure sensors on the fuselage of the GoAHEAD experiment. (Sensors evaluated in detail are marked in red and named pursuant to GoAHEAD notation)

sensors location was interpolated onto the sensor position using the 4 nearest given cell values. The experimental record covers 32 rotor revolution with a sampling frequency of $2035.2\,\mathrm{Hz}$. Representative for the area of concern for the tail shake phenomenon, three sensors placed at the tail boom and at the vertical fin (cf. figure 11) are pulled up for a detailed comparison between CFD and experimental data. They are compared with the phase averaged time development and with the frequency spectrum of the raw measured data. The standard deviation is shown in the time domain development to characterize the scattering of the data. For clarity, the comparison is limited to the experimental data and WENO-HLLC computation which showed best results so far. First,

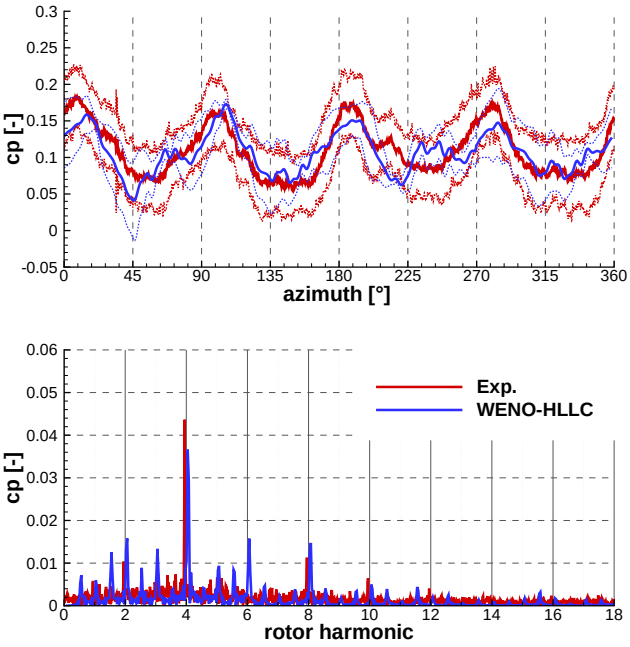

Fig. 12. Time development of phase averaged pressure data and frequency spectrum the raw data of the sensor K38 located at the tail boom.

the sensor denoted with K38 is considered, which is placed at the flow averted side of the tail boom. The time domain developments are shown in figure 12 over the azimuth of the main rotor. The developments are dominated by the 4/rev frequency with satisfying accordance in the amplitude strength. Beside the 4/rev frequency oscillation, higher harmonic frequency parts are mapped in the WENO-HLLC data as in the experimental data. Except a marginal runaway at 45° and 270° the WENO-HLLC data and its standard deviation is completely captured by the scattering of the experimental data.

Analyzing the frequency spectrum of the sensor, the 4th main rotor harmonic frequency, equaling the first blade passing frequency, characterizes the development. The reason for the occurrence of lower harmonics of the rotor in the CFD data is inter alia caused by the rotor hub and discussed in detail in section 5.2. In the 6th harmonic a significant higher amplitude is found in the WENO-HLLC data. Higher frequencies show reasonable accordance between WENO-HLLC and the experiment especially for the 8th, 10th and 12th harmonic.

The sensor's characteristic is congruent with the characteristic of the integral fuselage force F_y, with a distribution of the occurring frequency parts over several rotor harmonics besides harmonics of the 4/rev. Furthermore the underestimated 4/rev frequency in the development of F_y is found as well in the characteristic of the sensor.

Contrary to the sensor K38, the sensor K41 is placed

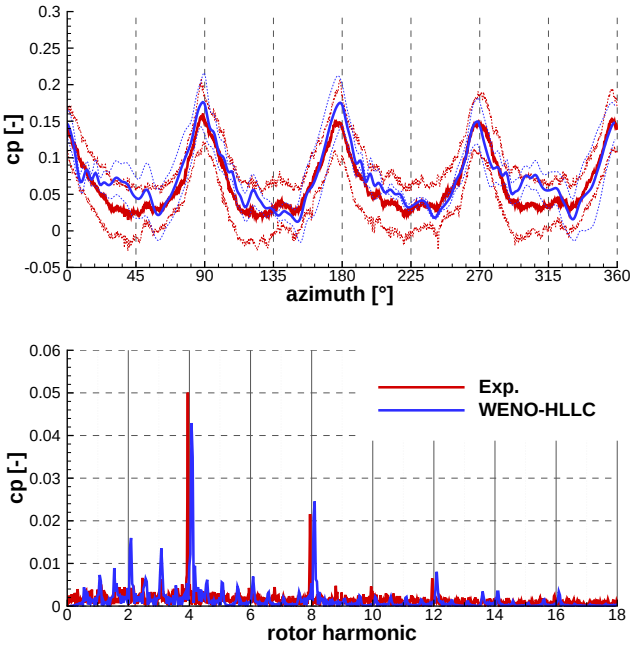

Fig. 13. Time development of phase averaged pressure data and frequency spectrum the raw data of the sensor K41 located at the tail boom.

normal under the rotor disk and faced to the rotor downwash. Thus the time development (cf. figure 13) shows a more distinct influence by the 4/rev rotor frequency dominating the pressure fluctuation. Remarkable are the accordances of the higher harmonic oscillation as it can be found at the lower peaks of the 4/rev oscillations in the vicinity of 45°, 135°, 225°, and 315°. The amplitudes, especially the harmonics of the 4/rev, have a high accordance in their strength as it can be seen in the frequency spectrum.

As for the sensor K38, the evaluation shows similar characteristics as the respective integral fuselage force, in case of sensor K41, F_x. Hence the phase shift of 20° is not found in the local pressure measurements.

The sensor K46 is chosen to evaluate the frequency spectrum of the incoming flow dominated by the rotor hub wake at the vertical fin (cf. figure 4). The pressure development of the sensor (cf. figure 14) shows a significant higher scattering of the frequency amplitudes over the spectrum. The time development shows deviations, hence with clearly the same trend with good compliance of the standard deviations. The frequency spectrum shows as well the same amplitude scale for nearly all occurring amplitudes. Only the 3rd, 6th, and 9th rotor harmonics are overestimated in their strength compared to the experiment. Considering the complex pressure development, a highly satisfying accordance be-

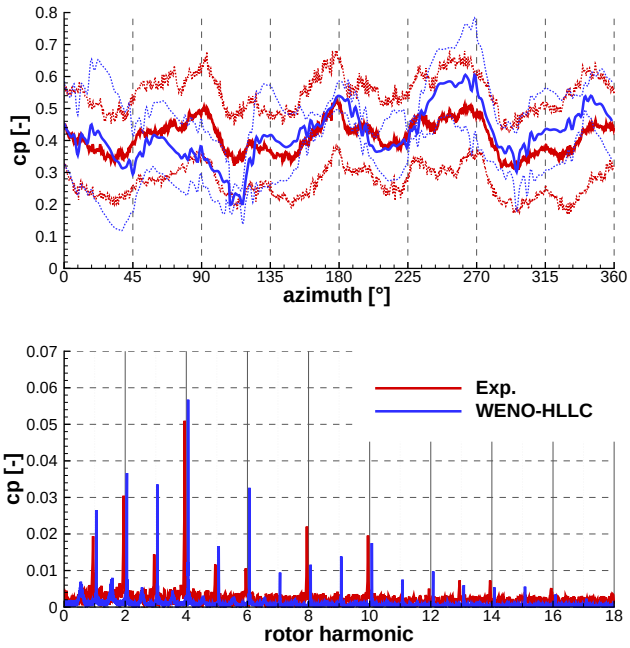

Fig. 14. Time development of phase averaged pressure data and frequency spectrum the raw data of the sensor K46 located at the tail fin.

tween the experiment and WENO-HLLC is achieved. Especially the 4/rev frequency influenced by the main rotor, and the 10/rev frequency by the tail rotor show high accordance. The combination of the 4/rev oscillation by the main rotor and 10/rev oscillation by the tail rotor leads to a 2/rev oscillation. This is presumed to be one reason for the occurrence of the 2/rev amplitude in the pressure distribution, which appears in the experimental data as well.
The higher mean pressure level is founded by the location of the pressure sensors K46 at the stagnation point of the tail fin. Which means, that beside pressure fluctuation in the incoming flow, the flow direction onto the tail fin influence the pressure level at the sensor. Hence it is expected that the characteristic of the pressure sensor reflects the flow field at the tail fin. A more precise investigation is presented in section 5.2.

A more general overview of the unsteady sensor measurements gives figure 15. The amplitude of the 4/rev fluctuation in the pressure coefficient for the experiment and the WENO-HLLC computation are shown over all pressure sensors. The plot displays the influence of the flow oscillation excited mainly by the main rotor. High influence can be found in the tail boom, especially on normal to the rotor disk located surfaces.
For a comparison between the experiment and the

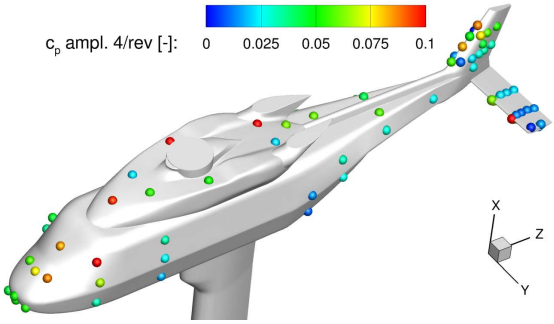

(a) GoAHEAD experiment

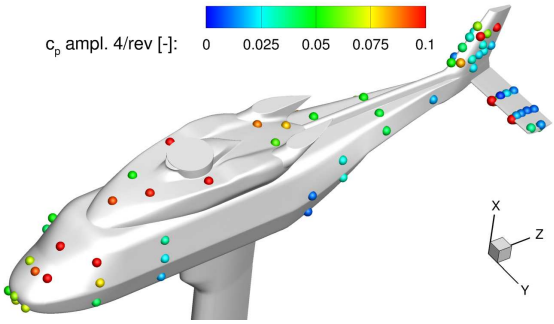

(b) WENO-HLLC computation

Fig. 15. 4/rev pressure amplitude of the sensor measurements.

WENO-HLLC computation, figure 16 shows the difference in the 4/rev pressure amplitude. The contour is log scaled to allow a more detailed rating of the deviation. Considering the pressure levels at the respective locations, the deviations are of a low scale in most regions.

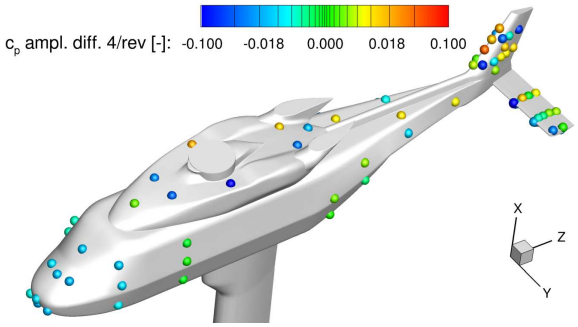

Fig. 16. Deviation of 4/rev amplitude between experimental data and WENO-HLLC computation. (Difference log scaled)

5.2 CFD data investigation

For a more detailed discussion of the rotor wake characteristics, figure 17 shows a slice through the rotor hub wake path with the normal vorticity $\frac{\delta v_1}{\delta x_2} - \frac{\delta v_2}{\delta x_1}$, with v_1 and v_2 as the in-plane velocity and x_1 and x_2, the plane coordinates. The stream traces show the

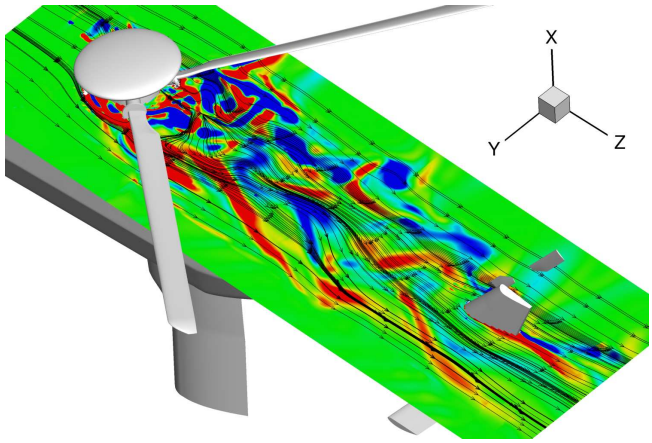

Fig. 17. Slice through the rotor hub wake path colored with the instantaneous normal vorticity and stream traces at the 16^{th} revolution and $\Psi = 45°$. (WENO-HLLC computation)

fluctuation of the wake characterized by periodically fluctuating vortices propagating downstream. The flow topology shows similar characteristics as a von Kármán vortex street around a cylinder with periodically detaching vortices, leading to the in-plane flow oscillation visualized by the stream traces. Leaving the blade connections out, the rotor hub equals

a cylinder with a diameter of $d = 0.31\,\mathrm{m}$. The inflow velocity of $v = 69.6\,\frac{\mathrm{m}}{\mathrm{s}}$ and a Reynolds number of $Re = 1.2e^6$ leads to a Strouhal number of $Sr = 0.215$ according to[14]. With

$$f = Sr\frac{v}{d}, \tag{2}$$

this leads to a frequency of the von Kármán vortex street of $48.27\,\mathrm{Hz}$. Considering the relation to the main rotor speed of $15.95\,\mathrm{Hz}$, the rotor hub wake characterized as a von Kármán vortex street coincides with the 3rd rotor harmonic fluctuation and multiples of it at the tail fin. Figure 18 shows the

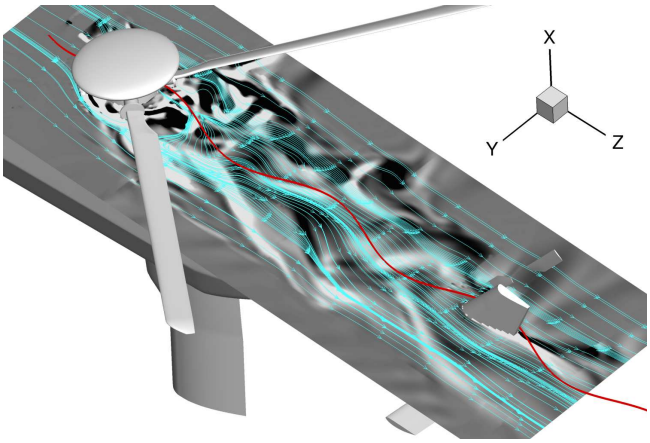

Fig. 18. Stream traces in the rotor hub wake path with an overlayed 3/rev oscillation at the 16^{th} revolution and $\Psi = 45°$. (WENO-HLLC computation)

overlay of the velocity stream traces with an in-plane 3/rev oscillation through the rotor hub center. The convective speed of the oscillation was set to the average convective speed of the wake, measured to $55\,\frac{\mathrm{m}}{\mathrm{s}}$. The comparison between the stream traces and the oscillation gradient show high accordance from the rotor hub until the approach at the tail fin. The appearance of the third rotor harmonic covers the characteristics of the frequency domain development of the sensors K46 as found in figure 14, which is located in the considered plane at the tail fin.

For a further investigation of the rotor hub wake influence onto the structure, the 3/rev pressure coefficient amplitudes of the considered sensor locations are plotted in figure 19. It can be clearly seen that an appearance of the frequency is located over the tail boom. Most influence is found at the tail fin, where the rotor hub wake interacts with the fuselage. For a quantification of the 3/rev amplitude part compared to the complete frequency spectrum, figure 20 shows the lateral force F_y of the tail fin. Contrary to the previous investigations, the integral value on the tail fin shows a higher amplitude in the 3/rev than in the 4/rev frequency. This shows the high influence of

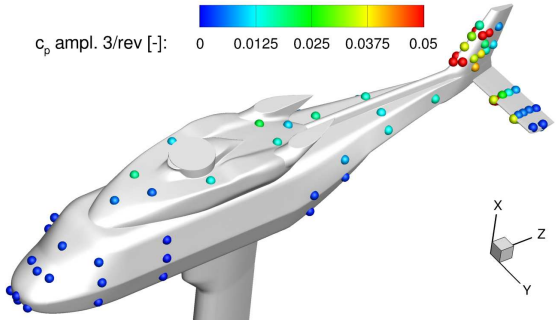

Fig. 19. 3/rev pressure coefficient amplitude of the sensor measurements. (WENO-HLLC computation)

the rotor wake, which was characterized to a 3/rev frequency. Due to the close location of the tail rotor, the 10/rev frequency is found as well with a high amplitude.

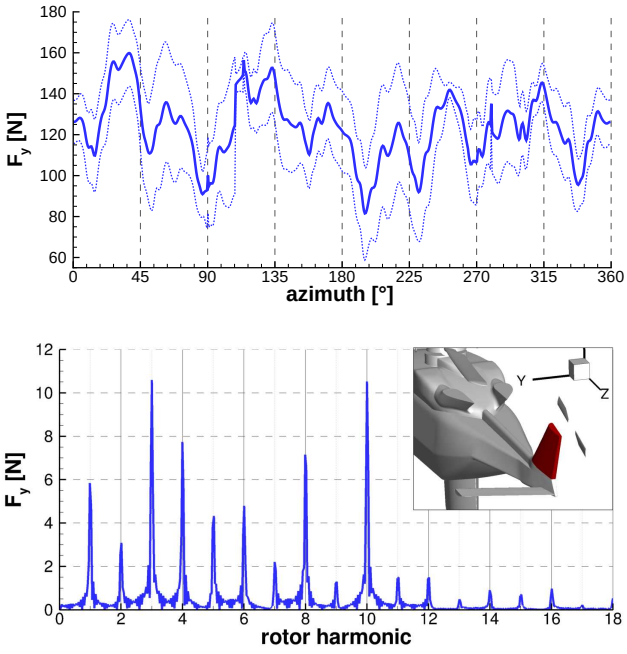

Fig. 20. Time development of phase averaged and frequency spectrum of the raw data of the lateral force F_y of the tail fin section. (WENO-HLLC computation)

In order to achieve more knowledge about the influence of the rotor wake including the rotor hub wake to the fuselage, the integral forces acting on the fuselage are pulled up once more. According to[1], the tail shake phenomenon is the result of the excitation of a lateral bending moment of the fuselage caused by the rotor hub wake. To investigate the characteristics of the influence onto the fuselage, figure 21 shows the moment M_x around the vertical axis of the fuselage, placed in the rotor mast.

Contrary to the investigated integral forces on the fuselage, the moment around the vertical axis shows another characteristic. The difference between the integral fuselage force and the moment result out of a time dependent shift of the point of load application. The previously investigated influence on the rotor hub wake to the tail boom is reflected in the moment with high influence of the 3/rev rotor harmonic. The frequency spectrum shows an influence of the 3/rev rotor harmonic in the scale of the second blade passing frequency and the tail rotor influence. Waard[1] estimates the first lateral bending moment causing the tail shake phenomenon in the vicinity of the 1 to 2/rev frequency for a full scale helicopter. Transferred to the conducted simulation, this frequency of concern for the tail shake phenomenon can be assigned to the found 3/rev rotor harmonic.

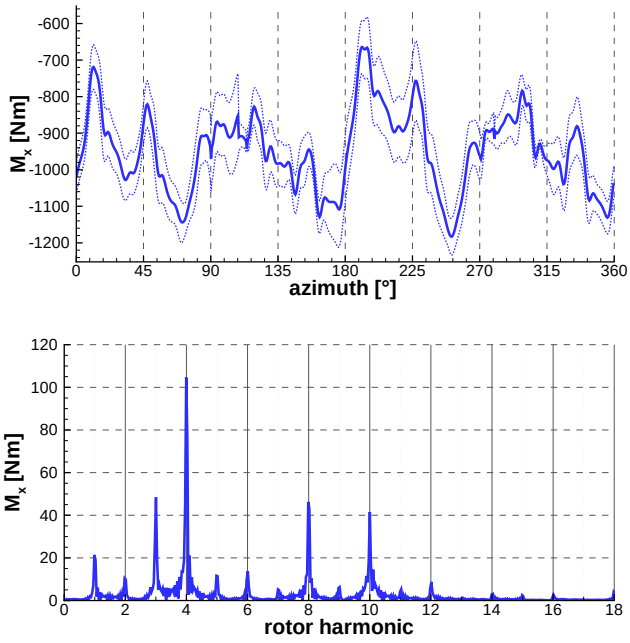

Fig. 21. Time development of phase averaged and frequency spectrum of the raw data of the fuselage moment M_x around the vertical axis located in the rotor mast. (WENO-HLLC computation)

6 CONCLUSION

The investigated tail shake flight condition of a comparison between the GoAHEAD wind tunnel test campaign with CFD simulation using different flux computation methods shows good results. Especially the usage of the higher order WENO method in combination with the HLLC Riemann solver achieved high accordance with the wind tunnel measurement data in several values. The integral fuselage forces show the same characteristics and scale in the vertical and lateral forces as the experimental data. The longitudinal force shows considerable deviations between the CFD simulations and experiment, whereby the accuracy of the experimental measurement is already questioned in the project reports. The comparison of the tail boom nearby area was conducted by a comparison of experimental PIV measurement data. The higher order method shows here advantage compared to the second order JST scheme. Hence the flow topology is not reproduced with satisfying accordance regarding the location of the vortices. The comparison of unsteady pressure sensors shows whereas high accordance in the time domain with a development of the WENO-HLLC computation amid the standard deviation of the experimental data. The frequency domain showed accordance as well, with a reliable reproduction of the distribution over the frequency spectrum. The comparison of the 4th rotor harmonic over all pressure sensor measurements provided by the experimental data shows satisfying accordance. Some differences between the amplitude values are found, but with comparably low deviation under consideration of the complex flow topology.

A detailed investigation of the rotor hub wake assuming the formation of a von Kármán vortex street enabled the detection of a 3/rev oscillation by the rotor hub wake at the tail fin. This was confirmed by the measurements at the tail boom as well as the integral force acting on the tail fin. The influence of this 3/rev oscillation was found to be a significant part in the moment around the vertical axis of the fuselage. Former investigations showed that the frequency of concern is in the vicinity of lower rotor harmonics than the blade passing frequency. The investigations in this paper confirms that a detailed modeling of the rotor hub is unavoidable considering rotor fuselage interactions in fast forward flight.

REFERENCES

[1] de Waard, P. and Trouv, M., *Tail shake vibration*, NLR-TP-99505, NLR, The Netherlands, 1999.

[2] Hassan, A., Thompson, T., Duque, E., and Melton, J., *Resolution of Tail Buffet Phenomenon for AH-64DTM Longbow Apace*, Proceedings of the 53rd Annual Forum of the American Helicopter Society, Virginia, USA, 1997.

[3] Kampa, K., Enenkl, B., Polz, G., and Roth, G., *Aeromechanic Aspects in the Design of the EC135*, Proceedings of the 23rd European Rotorcraft Forum, Dresden, Germany, 1997.

[4] Kroll, N., Eisfeld, B., and Bleeke, H., "The Navier-Stokes code FLOWer," *Notes on Numerical Fluid Mechanics*, 1999, pp. 58–71.

[5] Pahlke, K., *The GOAHEAD project*, Proceedings of the 33rd European Rotorcraft Forum, Kazan, Russia, 2007.

[6] Jameson, A., Schmidt, W., and Turkel, E., *Numerical Solution of the Euler Equations by Finite Volume Methods Using Runge-Kutta Time-Stepping Schemes*, 14th AIAA Fluid and Plasma Dynamic Conference, Palo Alto, California, USA, 1984.

[7] Jiang, G.-S. and Shu, C.-W., "Efficient Implementation of Weighted ENO Schemes," *Journal of Computational Physics*, Vol. 126, 1996, pp. 202–228.

[8] Toro, E. F., *Riemann Solvers and Numerical Methods for Fluid Dynamics*, Springer-Verlag, Berlin, 1997.

[9] Flad, D., *Implementation of a higher order method for flux calculation in FLOWer*, Studienarbeit, Institute of Aerodynamics and Gasdynamics, University of Stuttgart, Germany, 2011.

[10] Kowarsch, U., Oehrle, C., Hollands, M., Keßler, M., and Krämer, E., *Computation of Helicopter Phenomena Using a Higher Order Method*, High Performance Computing in Science and Engineering, Stuttgart, 2013, accepted.

[11] Wilcox, D., *Turbulence Modeling for CFD*, DCW Industries, Inc., München, 3nd edn., 2006.

[12] Benoit, B., Dequin, A.-M., von Grünhagen, W., Kampa, K., Basset, P.-M., and Gimonet, B., *HOST, a General Helicopter Simulation Tool for Germany and France*, Proceedings of the 56rd Annual Forum of the American Helicopter Society, Virginia, USA, 2000.

[13] Dietz, M., *Simulation der Aerodynamik von Hubschrauberkonfigurationen unter Berücksichtigung von Strömungs-Struktur-Kopplung und Trimmung*, PhD thesis, University of Stuttgart, 2008.

[14] Roshko, A., "Experiments on the Mean Flow Past a Circular Cylinder at Very High Reynolds Number," *Journal of Fluid Mechanics*, Vol. 10, 1961, pp. 345–356.

Appendix

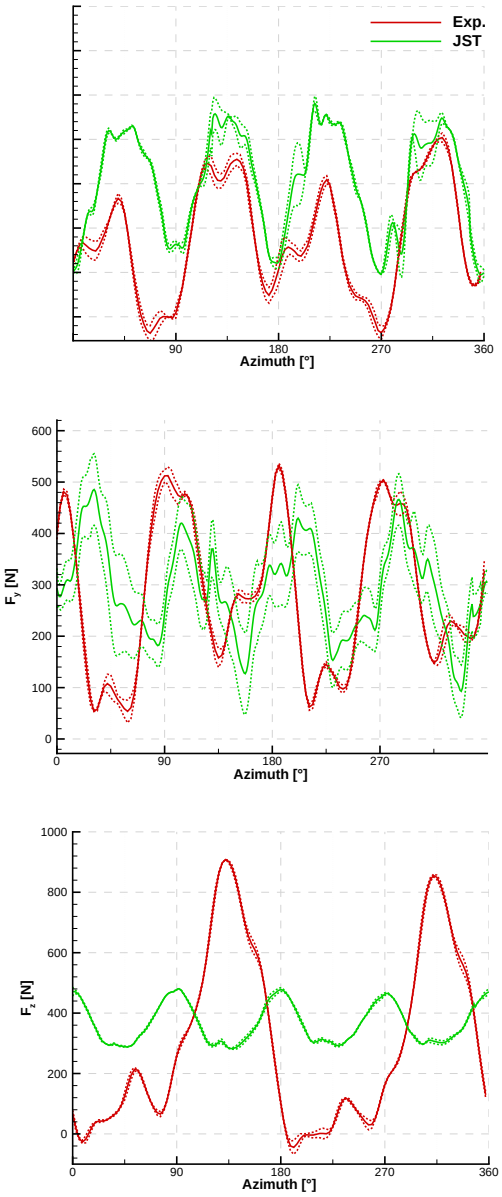

Fig. 22. Standard deviation of the phase averaged integral fuselage forces.